SARS-CoV-2 spike P681R mutation, a hallmark of the Delta variant, enhances viral fusogenicity and pathogenicity

Akatsuki Saito[1,2,3,#], Takashi Irie[4,#], Rigel Suzuki[5,#], Tadashi Maemura[6,7#], Hesham Nasser[8,9,#], Keiya Uriu[10,#], Yusuke Kosugi[10,#], Kotaro Shirakawa[11], Kenji Sadamasu[12], Izumi Kimura[10], Jumpei Ito[10], Jiaqi Wu[13,14], Kiyoko Iwatsuki-Horimoto[6], Mutsumi Ito[6], Seiya Yamayoshi[6,15], Seiya Ozono[16], Erika P Butlertanaka[1], Yuri L Tanaka[1], Ryo Shimizu[8,17], Kenta Shimizu[5], Kumiko Yoshimatsu[18], Ryoko Kawabata[4], Takemasa Sakaguchi[4], Kenzo Tokunaga[16], Isao Yoshida[12], Hiroyuki Asakura[12], Mami Nagashima[12], Yasuhiro Kazuma[11], Ryosuke Nomura[11], Yoshihito Horisawa[11], Kazuhisa Yoshimura[12], Akifumi Takaori-Kondo[11], Masaki Imai[6,15], The Genotype to Phenotype Japan (G2P-Japan) Consortium, So Nakagawa[13,14]*, Terumasa Ikeda[8]*, Takasuke Fukuhara[5]*, Yoshihiro Kawaoka[6,7,15]*, Kei Sato[8,12]*

[1] Department of Veterinary Science, Faculty of Agriculture, University of Miyazaki, Miyazaki 8892192, Japan
[2] Center for Animal Disease Control, University of Miyazaki, Miyazaki 8892192, Japan
[3] Graduate School of Medicine and Veterinary Medicine, University of Miyazaki, Miyazaki 8892192, Japan
[4] Institute of Biomedical and Health Sciences, Hiroshima University, Hiroshima 7348551, Japan
[5] Department of Microbiology and Immunology, Graduate School of Medicine, Hokkaido University, Hokkaido 0608638, Japan
[6] Division of Virology, Institute of Medical Science, University of Tokyo, Tokyo 1088639, Japan
[7] Influenza Research Institute, Department of Pathobiological Sciences, School of Veterinary Medicine, University of Wisconsin-Madison, WI 53711, USA
[8] Division of Molecular Virology and Genetics, Joint Research Center for Human Retrovirus infection, Kumamoto University, Kumamoto 8600811, Japan
[9] Department of Clinical Pathology, Faculty of Medicine, Suez Canal University, Ismailia 41511, Egypt
[10] Division of Systems Virology, Department of Infectious Disease Control, International Research Center for Infectious Diseases, The Institute of Medical Science, The University of Tokyo, Tokyo 1088639, Japan
[11] Department of Hematology and Oncology, Graduate School of Medicine, Kyoto University, Kyoto 6068507, Japan
[12] Tokyo Metropolitan Institute of Public Health, Tokyo 1690073, Japan
[13] Department of Molecular Life Science, Tokai University School of Medicine, Kanagawa 2591193, Japan

[14] CREST, Japan Science and Technology Agency, Saitama 3220012, Japan
[15] The Research Center for Global Viral Diseases, National Center for Global Health and Medicine Research Institute, Tokyo 1628655, Japan
[16] Department of Pathology, National Institute of Infectious Diseases, Tokyo 1628640, Japan
[17] Graduate School of Medical Sciences, Kumamoto University, Kumamoto 8600811, Japan
[18] Institute for Genetic Medicine, Hokkaido University, Hokkaido 0600815, Japan

[#] These authors contributed equally
*Correspondences:
so@tokai.ac.jp (S.N.)
ikedat@kumamoto-u.ac.jp (T.Ikeda)
fukut@pop.med.hokudai.ac.jp (T.F)
yoshihiro.kawaoka@wisc.edu (Y.Kawaoka)
KeiSato@g.ecc.u-tokyo.ac.jp (K.Sato)

Conflict of interest: The authors declare that no competing interests exist.
Keywords: SARS-CoV-2; COVID-19; spike protein; B.1.617.2; Delta variant; P681R; fusion

Abstract

During the current SARS-CoV-2 pandemic, a variety of mutations have been accumulated in the viral genome, and currently, four variants of concerns (VOCs) are considered as the hazardous SARS-CoV-2 variants to the human society[1]. The newly emerging VOC, the B.1.617.2/Delta variant, closely associates with a huge COVID-19 surge in India in Spring 2021[2]. However, its virological property remains unclear. Here, we show that the B.1.617.2/Delta variant is highly fusogenic, and notably, more pathogenic than prototypic SARS-CoV-2 in infected hamsters. The P681R mutation in the spike protein, which is highly conserved in this lineage, facilitates the spike protein cleavage and enhances viral fusogenicity. Moreover, we demonstrate that the P681R-bearing virus exhibits higher pathogenicity than the parental virus. Our data suggest that the P681R mutation is a hallmark that characterizes the virological phenotype of the B.1.617.2/Delta variant and is closely associated with enhanced pathogenicity.

Main

In December 2019, an unusual infectious disease, now called COVID-19, emerged in Wuhan, Hubei province, China[3,4]. SARS-CoV-2, the causative agent of COVID-19, has rapidly spread all over the world, and as of July 2021, SARS-CoV-2 is an ongoing pandemic: more than 180 million cases of infections have been reported worldwide, and more than 4 million people died of COVID-19[1].

During the current pandemic, SARS-CoV-2 has acquired a variety of mutations[5]. First, in the spring of 2020, a SARS-CoV-2 derivative harbouring the D614G mutation in its spike (S) protein has emerged and quickly become predominant[6]. Because the D614G mutation increases viral infectivity, fitness, and inter-individual transmissibility[7-12], the D614G-bearing variant has quickly swept out the original strain. Since the fall of 2020, some SARS-CoV-2 variants bearing multiple mutations have emerged and rapidly spread worldwide. As of June 2021, there have been at least five variants of concern (VOC): B.1.1.7 (Alpha), B.1.351 (Beta), P.1 (Gamma), B.1.427/429 (Epsilon; note that this variant is currently out of concerns/interest) and B.1.617.2 (Delta), and these lineages respectively emerged in the UK, South Africa, Brazil, the USA and India[13,14].

At the end of 2020, the B.1.617 lineage has emerged in India, and this variant is thought to be a main driver of a massive COVID-19 surge in India, which has peaked 400,000 infection cases per day[2]. The B.1.617 lineage includes three sublineages, B.1.617.1, B.1.617.2 and B.1.617.3, and a sublineage, B.1.617.2, is the latest VOC, the Delta variant[13,14]. Importantly, early evidence have suggested that the B.1.617.2/Delta may have an increased risk of hospitalization compared to the B.1.1.7 cases[15,16]. However, the virological features of this newly emerging VOC, particularly its infectivity and pathogenicity, remain unclear. Additionally, although recent studies have shown that the B.1.617.2/Delta variant is relatively resistant to the neutralising antibodies (NAbs) elicited by vaccination[17,18], the mutation(s) that are responsible for the virological features of this VOC are unaddressed. In this study, we demonstrate that the B.1.617.2/Delta is more pathogenic than the prototypic SARS-CoV-2 in a Syrian hamster model. We also show that the P681R mutation in the S protein is a hallmark mutation of this lineage. The P681R mutation enhances the cleavage of SARS-CoV-2 S protein and enhances viral fusogenicity. Moreover, we demonstrate that the P681R mutation is responsible for the higher pathogenicity of the B.1.617.2/Delta variant *in vivo*.

Phylogenetic and epidemic dynamics of the B.1.617 lineage

We set out to investigate the phylogenetic relationship of the three subvariants belonging to the B.1.617 lineage. We downloaded 1,761,037 SARS-CoV-2 genomes

113 and information data from the Global Initiative on Sharing All Influenza Data
114 (GISAID) database (https://www.gisaid.org; as of May 31, 2021). As expected, each
115 of three sublineages, B.1.617.1, B.1.617.2 and B.1.617.3, formed a monophyletic
116 cluster, respectively (**Fig. 1a, Extended Data Fig. 1**). We then analyzed the
117 epidemic of each of three B.1.617 sublineages. The B.1.617 variant, particularly
118 B.1.617.1, was first detected in India on December 1, 2020 (GISAID ID:
119 EPI_ISL_1372093) (**Fig. 1b-d**). Note that a SARS-CoV-2 variant (GISAID ID:
120 EPI_ISL_2220643) isolated in Texas, the USA, on August 10, 2020, was also
121 recorded to belong to the B.1.617.1. However, the S protein of this viral sequence
122 (GISAID ID: EPI_ISL_2220643) possesses neither L452R nor P681R mutations,
123 both of which are the features of the B.1.617 lineage. Therefore, the
124 EPI_ISL_2220643 sequence isolated in the USA may not be the ancestor of the
125 current B.1.617.1 lineage, and the EPI_ISL_1372093 sequence obtained in India
126 would be the oldest B.1.617 lineage.
127 The B.1.617.2 (GISAID ID: EPI_ISL_2131509) and B.1.617.3 (GISAID IDs:
128 EPI_ISL_1703672, EPI_ISL_1703659, EPI_ISL_1704392) were detected in India on
129 December 10, 2020 and February 13, 2021, respectively (**Fig. 1e, f**). The B.1.617.1
130 sublineage has peaked during February to April, 2021, in India, and then decreased
131 (**Fig. 1d**). Although the B.1.617.3 variant has sporadically detected in India (**Fig. 1f**),
132 the B.1.617.2/Delta lineage has become dominant in India since March 2021 and
133 spread all over the world (**Fig. 1e**). At the end of May 2021, 100%, 70% and 43.3%
134 of the deposited sequences in GISAID per day from India (May 7), the UK (May 21)
135 and the whole world (May 19) have been occupied by the B.1.617.2 sublineage (**Fig.
136 1e and Extended Data Table 1**).
137 We next investigated the proportion of amino acid replacements in the S
138 protein of each B.1.617 sublineage comparing with the reference strain (Wuhan-Hu-
139 1; GenBank accession no. NC_045512.2). As shown in **Fig. 1g**, the L452R and
140 P681R mutations were highly conserved in the B.1.617 lineage, and notably, the
141 P681R mutation (16,650/16,759 sequences, 99.3%) was the most representative
142 mutation in this lineage. These data suggest that the P681R mutation is a hallmark
143 of the B.1.617 lineage.
144
145 **Prominent syncytia formation by the B.1.617.2/Delta variant**
146 To investigate the virological characteristics of the B.1.617.2/Delta variant, we
147 conducted virological experiments using a viral isolate of B.1.617.2 (GISAID ID:
148 EPI_ISL_2378732) as well as a D614G-bearing B.1.1 isolate (GISAID ID:
149 EPI_ISL_479681) in Japan. In Vero cells, the growth of the B.1.617.2/Delta variant
150 was significantly lower than that of the B.1.1 isolate (**Fig. 2a**). Particularly, the levels

151 of viral RNA of the B.1.617.2/Delta variant at 48 hours postinfection (hpi) was more
152 than 150-fold lower than that of the B.1.1 isolate (**Fig. 2a**). On the other hand,
153 although the growth kinetics of these viruses was relatively comparable in
154 VeroE6/TMPRSS2 cells and Calu-3 cells (**Fig. 2a**), microscopic observations
155 showed that the B.1.617.2/Delta formed larger syncytia compared to the B.1.1 virus
156 (**Fig. 2b**). By measuring the size of the floating syncytia in the infected
157 VeroE6/TMPRSS2 culture, the syncytia formed by the B.1.617.2/Delta infection
158 were significantly (2.7-fold) larger than that by the B.1.1 infection (**Fig. 2b**).
159 Immunofluorescence assay further showed that the B.1.617.2/Delta-infected
160 VeroE6/TMPRSS2 cells exhibit larger multinuclear syncytia compared to the B.1.1
161 isolate (**Extended Data Fig. 2**). These results suggest that the B.1.617.2/Delta
162 variant is feasible for forming syncytia compared to the D614G-bearing B.1.1 virus.
163
164 **Higher pathogenicity of the B.1.617.2/Delta variant in Syrian hamsters**
165 To investigate the pathogenicity of the B.1.617.2/Delta variant, we conducted
166 hamster infection experiments using the B.1.617.2/Delta isolate and the B.1.1 isolate.
167 Although the viral RNA loads in the oral swab of the B.1.617.2/Delta-infected
168 hamsters were significantly lower than those of the B.1.1-infected hamsters at 1 and
169 4 days postinfection (dpi), these values were comparable any other dpi (**Fig. 2c**).
170 After infection with these viruses, infected hamsters significantly lost their body
171 weights from 2 dpi. The peak weight loss was 16% for the B.1.617.2/Delta and 13%
172 for the B.1.1, with the B.1.617.2/Delta isolate having a significantly greater weight
173 loss than the B.1.1 at 3 and 4 dpi (**Fig. 2d**). These results suggest that the
174 B.1.617.2/Delta has a higher pathogenicity than the B.1.1 isolate, despite relatively
175 comparable proliferative potential.
176
177 **P681R mutation as the determinant of enhanced and accelerated fusogenicity**
178 The P681R mutation in the S protein is a unique feature of the B.1.617 lineage
179 including the B.1.617.2/Delta variant (**Fig. 1g**). Because the P681R mutation is
180 located in the proximity of the furin cleavage site (FCS; residues RRAR positioned
181 between 682-5) of the SARS-CoV-2 S protein[19], we hypothesized that the P681R
182 mutation is responsible for the preference of cell-cell fusion, which leads to larger
183 syncytia formation. To address this possibility, we generated the P681R-bearing
184 artificial virus by reverse genetics (**Extended Data Fig. 3**) and preformed virological
185 experiments. Although the amounts of viral RNA in the culture supernatants of the
186 D614G/P681R-infected Vero and VeroE6/TMPRSS2 cells were significantly lower
187 than those of the D614G-infected cells in some time points, the growth of these two
188 viruses was relatively comparable (**Fig. 3a**). However, the size of floating syncytia in

189 the D614G/P681R-infected VeroE6/TMPRSS2 cells at 72 hpi was significantly larger
190 than that in the D614G mutant-infected cells (**Fig. 3b**). This observation well
191 corresponds to that in the culture infected with the B.1.617.2/Delta variant (**Fig. 2b**).
192 To clearly observe the syncytia formation, we further generated the GFP-
193 expressing replication-competent D614G and D614G/P681R viruses. The levels of
194 viral RNA in the supernatant and GFP-positive cells were similar in Vero,
195 VeroE6/TMPRSS2 and Calu-3 cells (**Extended Data Fig. 4**). However, at 24 hpi,
196 significantly larger GFP-positive adherent syncytia were observed in the
197 VeroE6/TMPRSS2 cells infected with the GFP-expressing D614G/P681R virus (**Fig.**
198 **3c**). Additionally, the size of GFP-positive floating syncytia at 72 hpi in the
199 VeroE6/TMPRSS2 cells infected with GFP-expressing D614G/P681R virus was
200 significantly bigger than that with GFP-expressing D614G virus (**Extended Data Fig.**
201 **5**). Moreover, GFP-positive syncytia were observed in the D614G/P681R-infected
202 but not in the D614G-infected Calu-3 cells at 72 hpi (**Extended Data Fig. 4c**). These
203 results suggest that the feature of the B.1.617.2/Delta virus observed in *in vitro* cell
204 culture experiments, particularly forming larger syncytia (**Fig. 2b** and **Extended Data**
205 **Fig. 2**), is well reproduced by the insertion of P681R mutation.
206 To directly investigate the effect of P681R mutation on the cleavage of
207 SARS-CoV-2 S protein, we prepared the HIV-1-based pseudoviruses carrying the
208 P681R mutation. Western blotting of the pseudoviruses prepared showed that the
209 level of cleaved S2 subunit was significantly increased by the P681R mutation
210 (**Extended Data Fig. 6a**), suggesting that the P681R mutation facilitates the furin-
211 mediated cleavage of SARS-CoV-2 S protein. We then performed the single-round
212 pseudovirus infection assay using the target HOS cells with or without TMPRSS2
213 expression. The infectivity of both the D614G and the D614G/P681R pseudoviruses
214 increased approximately 10-fold by the expression of TMPRSS2 in target cells
215 (**Extended Data Fig. 6b**). However, the infectivity of the D614G and the
216 D614G/P681R pseudoviruses were comparable regardless of TMPRSS2
217 expression (**Extended Data Fig. 6b**). These data suggest that the P681R mutation
218 does not affect the infectivity of viral particles.
219 We next addressed the effect of P681R mutation on viral fusogenicity by
220 cell-based fusion assay. In the effector cells (i.e., S-expressing cells), although the
221 expression level of the D614G/P681R S protein was comparable to that of the
222 D614G S, the level of the cleaved S2 subunit of the D614G/P681R mutant was
223 significantly higher than that of the D614G S (**Fig. 3d**). Consistent with the results in
224 the pseudovirus assay (**Extended Data Fig. 6**), these results suggest that P681R
225 mutation facilitates the S cleavage. Flow cytometry showed that the surface
226 expression level of the D614G/P681R S was significantly lower than the D614G S

227 (**Extended Data Fig. 7**). Nevertheless, the cell-based fusion assay using the target
228 cells without TMPRSS2 demonstrated that the D614G/P681R S is 2.1-fold more
229 fusogenic than the D614G S with a statistical significance (P = 0.0002 by Welch's t
230 test) (**Fig. 3e**). Moreover, a mathematical modeling analysis of the fusion assay data
231 showed that the initial fusion velocity of the D614G/P681R S (0.83 ± 0.03 per hour)
232 is significantly (2.8-fold) faster than that of the D614G S (0.30 ± 0.03 per hour; P =
233 4.0×10^{-6} by Welch's t test) (**Fig. 3f, g**). These data suggest that the P681R mutation
234 enhances and accelerates the SARS-CoV-2 S-mediated fusion. Furthermore, when
235 we use the target cells with TMPRSS2 expression, both the fusion efficacy (~1.2-
236 fold) and initial fusion velocity (~2.0-fold) were increased in both the D614G and
237 D614G/P681R S proteins (**Fig. 3f, g**). These results suggest that TMPRSS2
238 facilitates the fusion mediated by SARS-CoV-2 S and human ACE2, while the
239 TMPRSS2-dependent acceleration and promotion of viral fusion is not specific for
240 the P681R mutant.
241
242 **Resistance to NAb-mediated antiviral immunity by the P681R mutation**
243 The resistance to the NAb in the sera of COVID-19 convalescents and vaccinated
244 individuals is a hallmark characteristic of the VOCs (reviewed in [20,21]), and it has
245 been recently showed that the B.1.617.2/Delta variant is relatively resistant to the
246 vaccine-induced neutralisation[17,18]. To ask whether the P681R mutation contributes
247 to this virological phenotype, we performed the neutralisation assay. The
248 D614G/P681R pseudovirus was partially (1.2-1.5-fold) resistant to the three
249 monoclonal antibodies targeting the receptor binding domain of SARS-CoV-2 S
250 protein (**Extended Data Fig. 8a**). Additionally, the neutralisation experiments using
251 the 19 sera of second BNT162b2 vaccination showed that the D614G/P681R
252 pseudovirus is significantly resistant to the vaccine-induced NAbs compared to the
253 D614G pseudovirus (P < 0.0001 by Wilcoxon matched-pairs signed rank test;
254 **Extended Data Fig. 8b and 9**). These results suggest that the P681R-bearing
255 pseudovirus is relatively resistant to NAbs. Notably, in contrast to the neutralising
256 activity against cell-free viruses, the SARS-CoV-2 S-based fusion assay showed that
257 cell-cell infection is strongly resistant to the NAbs and the insensitivity to the NAbs
258 on cell-cell infection is not dependent on the P681R mutation (**Extended Data Fig.
259 8c**). Altogether, these findings suggest that the P681R mutation confers the NAbs
260 resistance upon cell-free viral particles and cell-cell infection is resistant to the NAb-
261 mediated antiviral action compared to cell-free infection.
262
263 **P681R mutation as the determinant of higher pathogenicity of the Delta variant**

264 To assess the impact of the P681R mutation on viral replication and the
265 pathogenicity of SARS-CoV-2, Syrian hamsters were intranasally infected with the
266 D614G and D614G/P681R viruses. The D614G-infected hamsters exhibited no
267 weight loss, although a slight decrease in body weight was observed for one of the
268 animals by 7 dpi (5.0%) (**Fig. 4a**). In contrast, all of hamsters infected with the
269 D614G/P681R virus experienced a gradual body weight loss and the animals
270 showed a significant weight loss of 4.7-6.9% at 7 dpi compared to the D614G virus
271 (P = 0.011, **Fig. 4a**). We also assessed pulmonary function in infected hamsters by
272 measuring enhanced pause (PenH), which is a surrogate marker for
273 bronchoconstriction or airway obstruction, by using a whole-body plethysmography
274 system. Syrian hamsters infected with the D614G and D614G/P681R viruses
275 showed the increases in the lung PenH value (**Fig. 4b**). At 7 dpi, the D614G/P681R-
276 infected animals had significantly higher PenH values compared with those of the
277 D614G-infected animals (P = 0.043). At 3 dpi, both viruses replicated efficiently in
278 the lungs and nasal turbinates of the infected animals and no significant difference
279 in viral replication was observed between the two groups (**Fig. 4c**). At 7 dpi, no
280 differences in viral titres in the nasal turbinates were found between the two groups;
281 however, the lung titres in the D614G/P681R-infected group were significantly higher
282 than those in the D614G-infected groups (P = 0.0013, **Fig. 4c**).
283
284 **Discussion**
285 Previous studies have demonstrated the close association of the FCS in the SARS-
286 CoV-2 S protein with viral replication mode and it is dependent on TMPRSS2.
287 Johnson et al. and Peacock et al. showed that the loss of FCS results in the increase
288 of viral replication efficacy in Vero cells while the attenuation of viral growth in the
289 Vero cells expressing TMPRSS2[22,23]. On the contrary, here we showed that the
290 replication efficacy of the B.1.617.2/Delta variant was severely decreased in Vero
291 cells compared to VeroE6/TMPRSS2 cells. More importantly, although the FCS-
292 deleted SARS-CoV-2 is less pathogenic than the parental virus[23], we revealed that
293 the B.1.617.2/Delta variant as well as the P681R-harbouring virus exhibit higher
294 pathogenicity. These findings suggest that the enhanced viral fusogenicity, which is
295 triggered by the P681R mutation, closely associates with viral pathogenicity.
296 It is evident that most VOCs considered so far have acquired mutations in
297 their S proteins, particularly in the RBD and N-terminal domain, to evade NAbs[20,21,24].
298 In sharp contrast, here we demonstrated that the B.1.617.2/Delta variant has
299 acquired a unique strategy to facilitate infection and evade antiviral immunity. The
300 P681R mutation that is highly conserved in this lineage enhances the efficacy of viral
301 fusion and further accelerates its speed of action. The P681R-mediated rapid

302 kinetics of viral fusion may attribute to not only immune evasion but also possibly
303 feasible the infection to exposed individuals.
304 Consistent with previous reports[25,26], here we showed that the cell-cell
305 infection mediated by the SARS-CoV-2 S protein is resistant to NAbs. The effect of
306 NAbs against cell-cell infection has been well studied in HIV-1 (*Retroviridae*)
307 infection, and it is well known that cell-cell infection is relatively more resistant to
308 NAbs compared to cell-free infection (reviewed in [27-29]). The resistance of cell-cell
309 spread against NAbs is not limited to HIV-1 but has been observed in the other
310 viruses such as vaccinia virus (*Poxviridae*)[30] and hepatitis C virus (*Flaviviridae*)[31],
311 suggesting that cell-cell infection is a common strategy for a variety of viruses to
312 evade antiviral humoral immunity. The fact that the B.1.617.2/Delta variant as well
313 as the P681R mutant efficiently form syncytia and the P681R mutant accelerates
314 and promotes cell-cell fusion suggests that switching the preference of viral
315 replication mode from cell-free infection to cell-cell infection may be a unique
316 strategy of the B.1.617.2/Delta variant to evade antiviral immunity.
317 Although the P681R mutant is highly fusogenic, the virus harbouring the
318 P681R mutation did not necessarily show higher growth compared to the parental
319 virus in *in vitro* cell cultures. Regarding this, the HIV-1 variants with higher
320 fusogenicity have been isolated from AIDS patients, but the enhanced fusogenicity
321 does not promote viral replication in *in vitro* cell cultures[32]. Similarly, the measles
322 virus (*Paramyxoviridae*) harbouring the deficient mutation in viral matrix protein[33]
323 and substitution mutations in viral fusion protein[34,35] are highly fusogenic and
324 efficiently expands via cell-cell fusion. However, the growth kinetics of these mutated
325 measles virus with higher fusogenicity in *in vitro* cell cultures is less efficient than the
326 parental virus[33]. Therefore, the discrepancy between the efficacy of viral growth in
327 *in vitro* cell cultures and viral fusogenicity is not specific for SARS-CoV-2. Rather,
328 the higher fusogenicity is associated with the severity of viral pathogenicity such as
329 HIV-1 encephalitis[36] and fatal subacute sclerosing panencephalitis, which is caused
330 by measles virus infection in brain[34,35]. Consistently, here we showed that the
331 B.1.617.2/Delta variant as well as the P681R mutant exhibited a higher fusogenicity
332 *in vitro* and enhanced pathogenicity *in vivo*. Our data suggest that the higher COVID-
333 19 severity and unusual symptoms caused by the B.1.617.2/Delta variant[15,16] are
334 partly due to the higher fusogenicity caused by the P681R mutation. Switching viral
335 infection mode by the P681R mutation may relate to the severity and/or unusual
336 outcome of viral infection, therefore, the epidemic of the SARS-CoV-2 variants
337 harbouring the P681R mutation should be surveyed in depth.

Author Contributions

A.S., T.Irie, R.Suzuki, H.N., K.U., Y.Kosugi, E.P.B., Y.L.T., R.Shimizu, K.Shimizu, R.K., T.Ikeda, T.F. and K.Sato performed the experiments.

R.Suzuki, T.M., K.I.-H., M.Ito, S.Y., M.Imai, K.Yoshimatsu, T.F. and Y.Kawaoka performed animal experiments.

K.Sadamasu, S.O., T.S., K.T., I.Y., H.A., M.N., and K.Yoshimura prepared experimental materials.

J.W. and S.N. performed molecular phylogenetic analysis.

K.Shirakawa, Y.Kazuma, R.N., Y.H., and A.T.-K. collected clinical samples.

A.S., T.Irie, M.Imai, S.N., T.Ikeda, T.F. Y.Kawaoka and K.S. designed the experiments and interpreted the results.

K.Sato wrote the original manuscript.

All authors reviewed and proofread the manuscript.

The Genotype to Phenotype Japan (G2P-Japan) Consortium contributed to the project administration.

Consortia

The Genotype to Phenotype Japan (G2P-Japan) Consortium: Mika Chiba, Hirotake Furihata, Haruyo Hasebe, Kazuko Kitazato, Haruko Kubo, Naoko Misawa, Nanami Morizako, Akiko Oide, Mai Suganami, Miyoko Takahashi, Kana Tsushima, Miyabishara Yokoyama, Yue Yuan

Acknowledgments

We would like to thank all members belonging to The Genotype to Phenotype Japan (G2P-Japan) Consortium. We thank Dr. Jin Gohda (The University of Tokyo, Japan) for providing reagents. An anti-HIV-1 p24 Monoclonal antibody (clone 183-H12-5C, Cat# ARP-3537) was obtained through the NIH HIV Reagent Program, NIAID, NIH (contributed by Drs. Bruce Chesebro and Kathy Wehrly). The super-computing resource was provided by Human Genome Center at The University of Tokyo and the NIG supercomputer at ROIS National Institute of Genetics.

This study was supported in part by AMED Research Program on Emerging and Re-emerging Infectious Diseases 20fk0108163 (to A.S.), 20fk0108401 (to T.F.), 21fk0108617 (to T.F.), 19fk0108113 (to Y.Kawaoka), JP20fk0108412 (to Y.Kawaoka), 20fk0108146 (to K.Sato), 20fk0108270 (to K.Sato) and 20fk0108413 (to T.Ikeda, S.N. and K.Sato); AMED Research Program on HIV/AIDS 21fk0410033 (to A.S.) and 21fk0410039 (to K.Sato); AMED Japan Program for Infectious Diseases Research and Infrastructure 20wm0325009 (to A.S.), 21wm0325009 (to A.S.) and 21wm0125002 (to Y.Kawaoka); JST A-STEP JPMJTM20SL (to T.Ikeda);

JST SICORP (e-ASIA) JPMJSC20U1 (to K.Sato); JST SICORP JPMJSC21U5 (to K.Sato), JST CREST JPMJCR20H6 (to S.N.) and JPMJCR20H4 (to K.Sato); JSPS KAKENHI Grant-in-Aid for Scientific Research C 19K06382 (to A.S.), 18K07156 (to K.T.) and 21K07060 (to K.T.), Scientific Research B 18H02662 (to K.Sato) and 21H02737 (to K.Sato); JSPS Fund for the Promotion of Joint International Research (Fostering Joint International Research) 18KK0447 (to K.Sato); JSPS Core-to-Core Program JPJSCCA20190008 (A. Advanced Research Networks) (to K.Sato); JSPS Research Fellow DC1 19J20488 (to I.K.); JSPS Leading Initiative for Excellent Young Researchers (LEADER) (to T.Ikeda); ONO Medical Research Foundation (to K.Sato); Ichiro Kanehara Foundation (to K.Sato); Lotte Foundation (to K.Sato); Mochida Memorial Foundation for Medical and Pharmaceutical Research (to K.Sato); Daiichi Sankyo Foundation of Life Science (to K.Sato); Sumitomo Foundation (to K.Sato); Uehara Foundation (to K.Sato); Takeda Science Foundation (to T.Ikeda and K.Sato); The Tokyo Biochemical Research Foundation (to K.Sato); Mitsubishi Foundation (to T.Ikeda); Shin-Nihon Foundation of Advanced Medical Research (to T.Ikeda); Tsuchiya Foundation (to T.Irie); a Grant for Joint Research Projects of the Research Institute for Microbial Diseases, Osaka University (to A.S.); an intramural grant from Kumamoto University COVID-19 Research Projects (AMABIE) (to T.Ikeda); Intercontinental Research and Educational Platform Aiming for Eradication of HIV/AIDS (to T.Ikeda); and Joint Usage/Research Center program of Institute for Frontier Life and Medical Sciences, Kyoto University (to K.Sato).

397 **References**

398 1 WHO. "Coronavirus disease 2019".
399 https://www.who.int/emergencies/diseases/novel-coronavirus-2019. (2021).
400 2 Singh, J., Rahman, S. A., Ehtesham, N. Z., Hira, S. & Hasnain, S. E. SARS-
401 CoV-2 variants of concern are emerging in India. *Nat Med*,
402 doi:10.1038/s41591-021-01397-4 (2021).
403 3 Wu, F. *et al.* A new coronavirus associated with human respiratory disease in
404 China. *Nature* **579**, 265-269, doi:10.1038/s41586-020-2008-3 (2020).
405 4 Zhou, P. *et al.* A pneumonia outbreak associated with a new coronavirus of
406 probable bat origin. *Nature* **579**, 270-273, doi:10.1038/s41586-020-2012-7
407 (2020).
408 5 Plante, J. A. *et al.* The variant gambit: COVID's next move. *Cell Host Microbe*
409 **29**, 508-515, doi:10.1016/j.chom.2021.02.020 (2021).
410 6 Korber, B. *et al.* Tracking changes in SARS-CoV-2 spike: evidence that
411 D614G increases infectivity of the COVID-19 virus. *Cell* **182**, 812-827,
412 doi:10.1016/j.cell.2020.06.043 (2020).
413 7 Zhou, B. *et al.* SARS-CoV-2 spike D614G change enhances replication and
414 transmission. *Nature* **592**, 122-127, doi:10.1038/s41586-021-03361-1 (2021).
415 8 Ozono, S. *et al.* SARS-CoV-2 D614G spike mutation increases entry
416 efficiency with enhanced ACE2-binding affinity. *Nat Commun* **12**, 848,
417 doi:10.1038/s41467-021-21118-2 (2021).
418 9 Yurkovetskiy, L. *et al.* Structural and functional analysis of the D614G SARS-
419 CoV-2 spike protein variant. *Cell* **183**, 739-751 e738,
420 doi:10.1016/j.cell.2020.09.032 (2020).
421 10 Hou, Y. J. *et al.* SARS-CoV-2 D614G variant exhibits efficient replication ex
422 vivo and transmission in vivo. *Science* **370**, 1464-1468,
423 doi:10.1126/science.abe8499 (2020).
424 11 Plante, J. A. *et al.* Spike mutation D614G alters SARS-CoV-2 fitness. *Nature*,
425 doi:10.1038/s41586-020-2895-3 (2020).
426 12 Volz, E. *et al.* Evaluating the effects of SARS-CoV-2 spike mutation D614G
427 on transmissibility and pathogenicity. *Cell* **184**, 64-75 e11,
428 doi:10.1016/j.cell.2020.11.020 (2021).
429 13 CDC. "SARS-CoV-2 variant classifications and definitions (updated June 10,
430 2021)". https://www.cdc.gov/coronavirus/2019-ncov/variants/variant-
431 info.html. (2021).
432 14 WHO. "Tracking SARS-CoV-2 variants".
433 https://www.who.int/en/activities/tracking-SARS-CoV-2-variants/. (2021).
434 15 PHE. Public Health England. "3 June 2021 Risk assessment for SARS-CoV-

435 2 variant: Delta (VOC-21APR-02, B.1.617.2)"
436 https://assets.publishing.service.gov.uk/government/uploads/system/upload
437 s/attachment_data/file/991135/3_June_2021_Risk_assessment_for_SARS-
438 CoV-2_variant_DELTA.pdf. (2021).
439 16 Sheikh, A. *et al.* SARS-CoV-2 Delta VOC in Scotland: demographics, risk of
440 hospital admission, and vaccine effectiveness. *Lancet* **397**, 2461-2462,
441 doi:10.1016/S0140-6736(21)01358-1 (2021).
442 17 Wall, E. C. *et al.* Neutralising antibody activity against SARS-CoV-2 VOCs
443 B.1.617.2 and B.1.351 by BNT162b2 vaccination. *Lancet*,
444 doi:10.1016/S0140-6736(21)01290-3 (2021).
445 18 Planas, D. *et al.* Reduced sensitivity of SARS-CoV-2 variant Delta to antibody
446 neutralization. *Nature*, doi:10.1038/s41586-021-03777-9 (2021).
447 19 Shang, J. *et al.* Cell entry mechanisms of SARS-CoV-2. *Proc Natl Acad Sci*
448 *U S A* **117**, 11727-11734, doi:10.1073/pnas.2003138117 (2020).
449 20 Harvey, W. T. *et al.* SARS-CoV-2 variants, spike mutations and immune
450 escape. *Nat Rev Microbiol*, doi:10.1038/s41579-021-00573-0 (2021).
451 21 Corti, D., Purcell, L. A., Snell, G. & Veesler, D. Tackling COVID-19 with
452 neutralizing monoclonal antibodies. *Cell*, doi:10.1016/j.cell.2021.05.005
453 (2021).
454 22 Peacock, T. P. *et al.* The furin cleavage site in the SARS-CoV-2 spike protein
455 is required for transmission in ferrets. *Nat Microbiol*, doi:10.1038/s41564-021-
456 00908-w (2021).
457 23 Johnson, B. A. *et al.* Loss of furin cleavage site attenuates SARS-CoV-2
458 pathogenesis. *Nature* **591**, 293-299, doi:10.1038/s41586-021-03237-4
459 (2021).
460 24 Piccoli, L. *et al.* Mapping Neutralizing and Immunodominant Sites on the
461 SARS-CoV-2 Spike Receptor-Binding Domain by Structure-Guided High-
462 Resolution Serology. *Cell* **183**, 1024-1042 e1021,
463 doi:10.1016/j.cell.2020.09.037 (2020).
464 25 Kruglova, N., Siniavin, A., Gushchin, V. & Mazurov, D. SARS-CoV-2 cell-to-
465 cell infection is resistant to neutralizing antibodies. *BioRxiv*, 442701 (2021).
466 26 Xia, S. *et al.* Inhibition of SARS-CoV-2 (previously 2019-nCoV) infection by a
467 highly potent pan-coronavirus fusion inhibitor targeting its spike protein that
468 harbors a high capacity to mediate membrane fusion. *Cell Res* **30**, 343-355,
469 doi:10.1038/s41422-020-0305-x (2020).
470 27 Dufloo, J., Bruel, T. & Schwartz, O. HIV-1 cell-to-cell transmission and broadly
471 neutralizing antibodies. *Retrovirology* **15**, 51, doi:10.1186/s12977-018-0434-
472 1 (2018).

473 28 Agosto, L. M., Uchil, P. D. & Mothes, W. HIV cell-to-cell transmission: effects
474 on pathogenesis and antiretroviral therapy. *Trends Microbiol* **23**, 289-295,
475 doi:10.1016/j.tim.2015.02.003 (2015).
476 29 Sattentau, Q. Avoiding the void: cell-to-cell spread of human viruses. *Nat Rev*
477 *Microbiol* **6**, 815-826, doi:10.1038/nrmicro1972 (2008).
478 30 Law, M., Hollinshead, R. & Smith, G. L. Antibody-sensitive and antibody-
479 resistant cell-to-cell spread by vaccinia virus: role of the A33R protein in
480 antibody-resistant spread. *J Gen Virol* **83**, 209-222, doi:10.1099/0022-1317-
481 83-1-209 (2002).
482 31 Timpe, J. M. *et al.* Hepatitis C virus cell-cell transmission in hepatoma cells in
483 the presence of neutralizing antibodies. *Hepatology* **47**, 17-24,
484 doi:10.1002/hep.21959 (2008).
485 32 Sterjovski, J. *et al.* Asn 362 in gp120 contributes to enhanced fusogenicity by
486 CCR5-restricted HIV-1 envelope glycoprotein variants from patients with
487 AIDS. *Retrovirology* **4**, 89, doi:10.1186/1742-4690-4-89 (2007).
488 33 Cathomen, T. *et al.* A matrix-less measles virus is infectious and elicits
489 extensive cell fusion: consequences for propagation in the brain. *EMBO J* **17**,
490 3899-3908, doi:10.1093/emboj/17.14.3899 (1998).
491 34 Ikegame, S. *et al.* Fitness selection of hyperfusogenic measles virus F
492 proteins associated with neuropathogenic phenotypes. *Proc Natl Acad Sci U*
493 *S A* **118**, doi:10.1073/pnas.2026027118 (2021).
494 35 Watanabe, S. *et al.* Mutant fusion proteins with enhanced fusion activity
495 promote measles virus spread in human neuronal cells and brains of suckling
496 hamsters. *J Virol* **87**, 2648-2659, doi:10.1128/JVI.02632-12 (2013).
497 36 Rossi, F. *et al.* The V1-V3 region of a brain-derived HIV-1 envelope
498 glycoprotein determines macrophage tropism, low CD4 dependence,
499 increased fusogenicity and altered sensitivity to entry inhibitors. *Retrovirology*
500 **5**, 89, doi:10.1186/1742-4690-5-89 (2008).
501 37 Matsuyama, S. *et al.* Enhanced isolation of SARS-CoV-2 by TMPRSS2-
502 expressing cells. *Proc Natl Acad Sci U S A* **117**, 7001-7003,
503 doi:10.1073/pnas.2002589117 (2020).
504 38 Ferreira, I. *et al.* SARS-CoV-2 B.1.617 emergence and sensitivity to vaccine-
505 elicited antibodies. *BioRxiv*, 443253 (2021).
506 39 Torii, S. *et al.* Establishment of a reverse genetics system for SARS-CoV-2
507 using circular polymerase extension reaction. *Cell Rep* **35**, 109014 (2021).
508 40 Katoh, K. & Standley, D. M. MAFFT multiple sequence alignment software
509 version 7: improvements in performance and usability. *Mol Biol Evol* **30**, 772-
510 780, doi:10.1093/molbev/mst010 (2013).

41 Minh, B. Q. *et al.* IQ-TREE 2: New Models and Efficient Methods for Phylogenetic Inference in the Genomic Era. *Mol Biol Evol* **37**, 1530-1534, doi:10.1093/molbev/msaa015 (2020).

42 Reed, L. J. & Muench, H. A Simple Method of Estimating Fifty Percent Endpoints. *Am J Hygiene* **27**, 493-497 (1938).

43 Motozono, C. *et al.* An emerging SARS-CoV-2 mutant evading cellular immunity and increasing viral infectivity. *BioRxiv*, 438288 (2021).

44 Rausch, T., Fritz, M. H., Untergasser, A. & Benes, V. Tracy: basecalling, alignment, assembly and deconvolution of sanger chromatogram trace files. *BMC Genomics* **21**, 230, doi:10.1186/s12864-020-6635-8 (2020).

45 Shema Mugisha, C. *et al.* A simplified quantitative real-time PCR assay for monitoring SARS-CoV-2 growth in cell culture. *mSphere* **5**, doi:10.1128/mSphere.00658-20 (2020).

46 Niwa, H., Yamamura, K. & Miyazaki, J. Efficient selection for high-expression transfectants with a novel eukaryotic vector. *Gene* **108**, 193-199, doi:10.1016/0378-1119(91)90434-d (1991).

47 Ozono, S., Zhang, Y., Tobiume, M., Kishigami, S. & Tokunaga, K. Super-rapid quantitation of the production of HIV-1 harboring a luminescent peptide tag. *J Biol Chem* **295**, 13023-13030, doi:10.1074/jbc.RA120.013887 (2020).

48 Ikeda, T. *et al.* HIV-1 restriction by endogenous APOBEC3G in the myeloid cell line THP-1. *J Gen Virol* **100**, 1140-1152, doi:10.1099/jgv.0.001276 (2019).

49 Ikeda, T. *et al.* HIV-1 adaptation studies reveal a novel Env-mediated homeostasis mechanism for evading lethal hypermutation by APOBEC3G. *PLoS Pathog* **14**, e1007010, doi:10.1371/journal.ppat.1007010 (2018).

50 Sultana, T. *et al.* Multiple Pathways To Avoid Beta Interferon Sensitivity of HIV-1 by Mutations in Capsid. *J Virol* **93**, doi:10.1128/JVI.00986-19 (2019).

51 Kondo, N., Miyauchi, K. & Matsuda, Z. Monitoring viral-mediated membrane fusion using fluorescent reporter methods. *Curr Protoc Cell Biol* **Chapter 26**, Unit 26 29, doi:10.1002/0471143030.cb2609s50 (2011).

Figures & figure legends

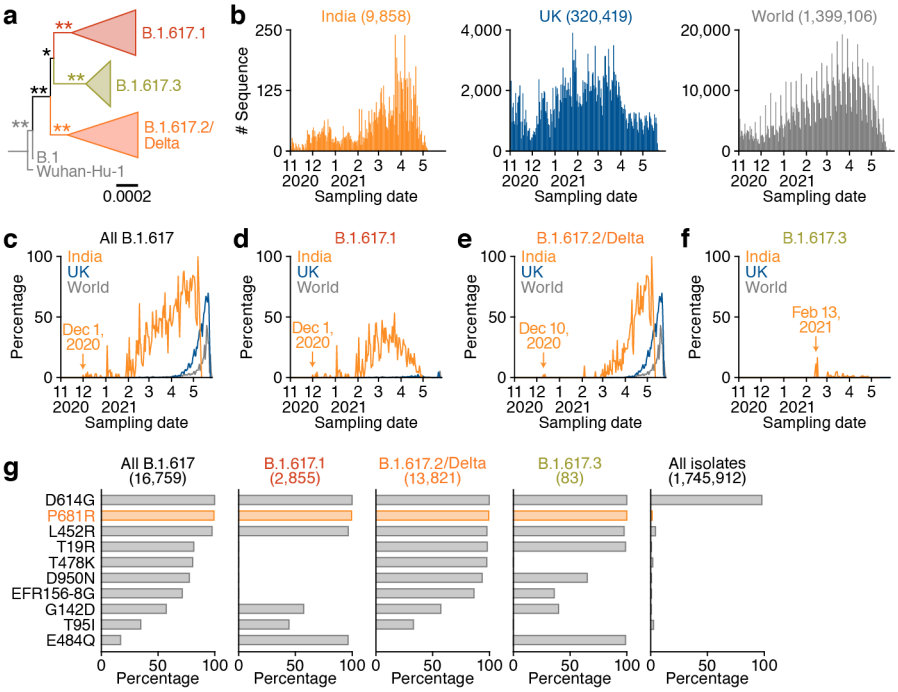

Fig. 1. Molecular phylogenetic and epidemic dynamics of the B.1.617 lineage during the pandemic.

a, A phylogenetic tree of the B.1.617 lineage. Bar, 0.0002 substitutions per site. Bootstrap values, **, 100%; *, >70%. The uncollapsed tree is shown in **Extended Data Fig. 1**.

b-f, Epidemic dynamics of the B.1.617 lineage. **b,** The numbers of sequences deposited in GISAID per day for India (orange, left), UK (blue, middle), and the whole world (gray, right). **c-f,** The percentages of each lineage deposited per day (**c**, all B.1.617; **d**, B.1.617.1; **e**, B.1.617.2/Delta; **f**, B.1.617.3) from India (orange), the UK (blue) and the whole world (gray) are shown. The date first identified is indicated. The raw data are summarized in **Extended Data Table 1**.

g, Proportion of amino acid replacements in the B.1.617 lineage. The top 10 replacements conserved in the S protein of the B.1.617 and its sublineages are summarized. The number in parenthesis indicates the number of sequences included in each panel. The raw data are summarized in **Extended Data Table 2**.

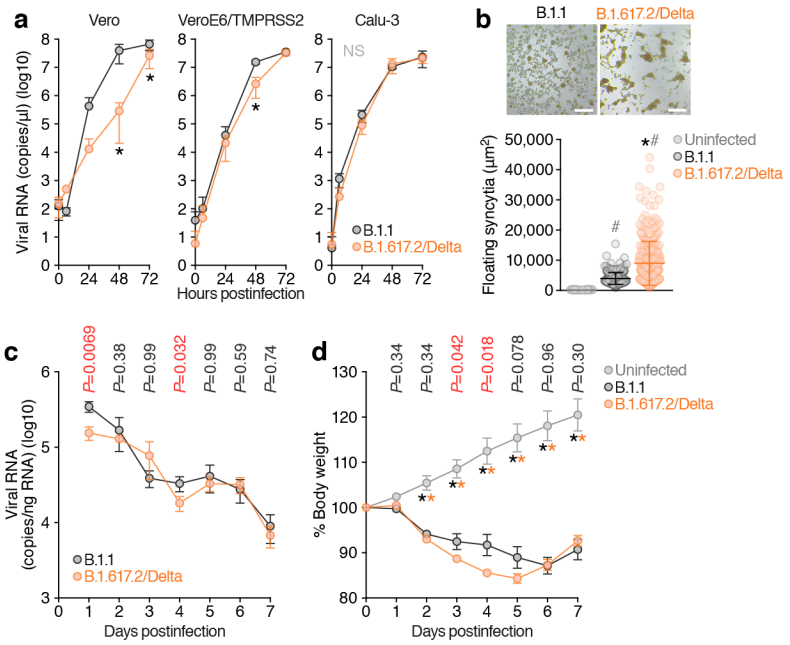

Fig. 2. Virological features of the B.1.617.2/Delta variant *in vitro* and *in vivo*.

a, Growth kinetics of the B.1.617.2/Delta variant and a B.1.1 isolate. A viral isolate of B.1.617.2/Delta (GISAID ID: EPI_ISL_2378732) and a D614G-bearing B.1.1 isolate (GISAID ID: EPI_ISL_479681) [100 50% tissue culture infectious dose ($TCID_{50}$) for Vero cells and VeroE6/TMPRSS2 cells, 1,000 $TCID_{50}$ for Calu-3 cells] were inoculated and the copy number of viral RNA in the culture supernatant was quantified by real-time RT-PCR. The growth curves of the viruses inoculated are shown. Assays were performed in quadruplicate.

b, Syncytia formation. The syncytia in infected VeroE6/TMPRSS2 cells were observed at 72 hpi. (Top) Representative bright-field images of VeroE6/TMPRSS2 cells at 72 hpi are shown. Bars, 100 μm. (Bottom) The size of floating syncytia in B.1.1-infected (n = 217) and B.1.617.2/Delta-infected (n = 217) cultures are shown. The size of the floating single cells in uninfected culture (n = 177) was also shown as a negative control.

c, d, Syrian hamster infection with the B.1.617.2/Delta variant. Male hamsters were infected with 10^5 $TCID_{50}$ of the B.1.1 isolate (n = 6) and the B.1.617.2/Delta isolate (n = 12). Four hamsters at the same age were used for mock infection. The amount of viral RNA in the oral swab (**c**) and body weight (**d**) and were routinely measured.

In **a**, statistically significant differences (*, $P < 0.05$) versus the B.1.1 isolate were determined by Student's *t* test. NS, no statistical significance.

In **b**, statistically significant differences versus the B.1.1-infected culture (*, $P < 0.05$) and uninfected culture (#, $P < 0.05$) were determined by the Mann-Whitney U test.

584 In **c** and **d**, statistically significant differences were determined by the Mann-Whitney
585 U test, and those versus uninfected hamsters (*, $P < 0.05$) are indicated by asterisks.
586 The P value between the B.1.1 and the B.1.617.2/Delta at each dpi is indicated in
587 the figure.

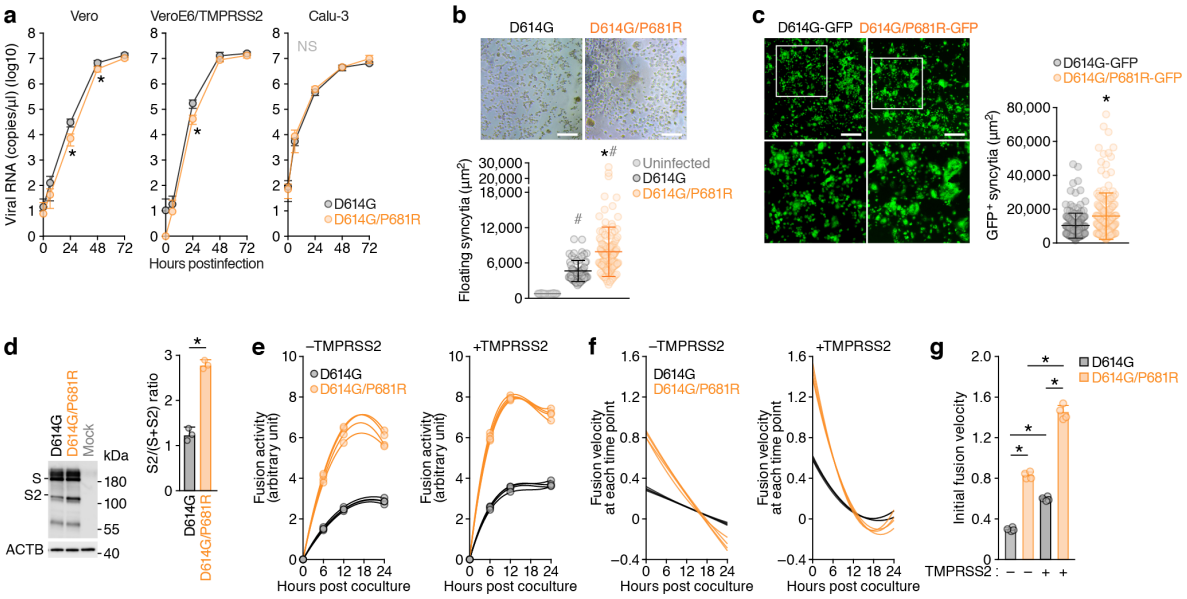

Fig. 3. Virological features of the P681R-harbouring virus *in vitro.*

a, Growth kinetics of artificially generated viruses. The D614G and D614G/P681R mutant viruses were generated by reverse genetics. These viruses (100 $TCID_{50}$) were inoculated into Vero cells and VeroE6/TMPRSS2 cells, and the copy number of viral RNA in the culture supernatant was quantified by real-time RT-PCR. The growth curves of the viruses inoculated are shown. Assays were performed in quadruplicate.

b, c, Syncytia formation. **b,** (Top) Floating syncytia in VeroE6/TMPRSS2 cells infected with the D614G and D614G/P681R mutant viruses at 72 hpi are shown. Bars, 200 μm. (Bottom) The size of floating syncytia in the D614G mutant-infected (n = 63) and the D614G/P681R mutant-infected (n = 126) cultures are shown. **c,** (Left) Adherent syncytia in VeroE6/TMPRSS2 cells infected with the GFP-expressing D614G and D614G/P681R mutant viruses at 24 hpi are shown. Areas enclosed with squares are enlarged in the bottom panels. Bars, 200 μm. (Right) The size of adherent GFP^+ syncytia in the D614G mutant-infected (n = 111) and the D614G/P681R mutant-infected (n = 126) cultures are shown.

d, Western blotting of the S-expressing cells. (Left) Representative blots of SARS-CoV-2 full-length S and cleaved S2 proteins as well as ACTB as an internal control. kDa, kilodalton. (Right) The ratio of S2 to the full-length S plus S2 proteins in the S-expressing cells.

e-g, SARS-CoV-2 S-based fusion assay. Effector cells (S-expressing cells) and target cells (ACE2-expressing cells or ACE2/TMPRSS2-expressing cells) were prepared, and the fusion activity was measured as described in **Methods**. **e,** Kinetics

613 of fusion activity (experimental data). Assays were performed in quadruplicate, and
614 fusion activity (arbitrary unit) is shown. **f,** The kinetics of fusion velocity estimated by
615 a mathematical model based on the kinetics of fusion activity data (see **Methods**).
616 **g,** Initial velocity of the S-mediated fusion.
617 In **b,c**, statistically significant differences versus the D614G mutant-infected culture
618 (*, $P < 0.05$) and uninfected culture (#, $P < 0.05$) were determined by the Mann-
619 Whitney U test.
620 In **d**, a statistically significant difference (*, $P < 0.05$) versus the D614G S was
621 determined by Student's *t* test.
622 In **g,** statistically significant differences (*, $P < 0.05$) were determined by two-sided
623 Welch's *t* test.

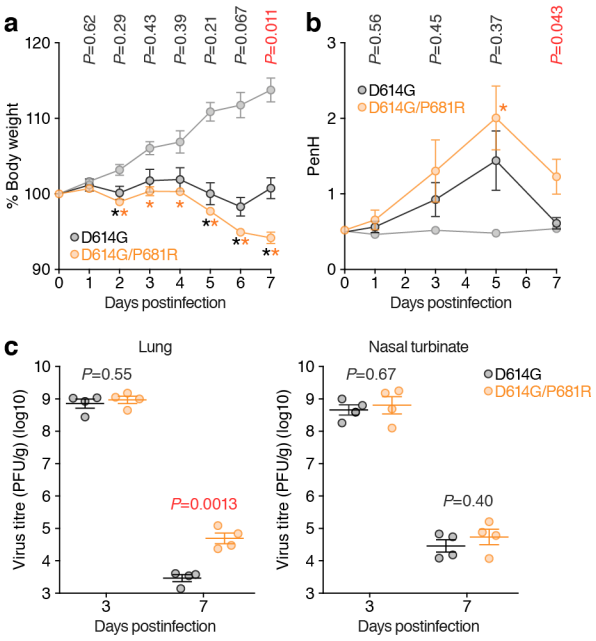

Fig. 4. Enhanced pathogenicity by the P681R mutation in hamsters.
Syrian hamsters were intranasally inoculated with 10^4 $TCID_{50}$ (in 30 μl) of the D614G and D614G/P681R viruses.
a, Body weight changes in hamsters after viral infection. Body weights of virus-infected (n = 4 each) and uninfected hamsters (n = 3) were monitored daily for 7 days.
b, Pulmonary function analysis in infected hamsters. Enhanced pause (PenH), which is a surrogate marker for bronchoconstriction or airway obstruction, was measured by using whole-body plethysmography.
c, Virus replication in infected hamsters. Four hamsters per group were euthanized at 3 and 7 dpi for virus titration. Virus titres in the lungs (left) nasal turbinates (right) were determined by the plaque assay using VeroE6/TMPRSS2 cells. Points indicate data from individual Syrian hamsters.
Statistically significant differences were determined by the Mann-Whitney U test, and those versus uninfected hamsters (*, $P < 0.05$) are indicated by asterisks. The P value between the D614G and the D614G/P681R at each dpi is indicated in the figure.

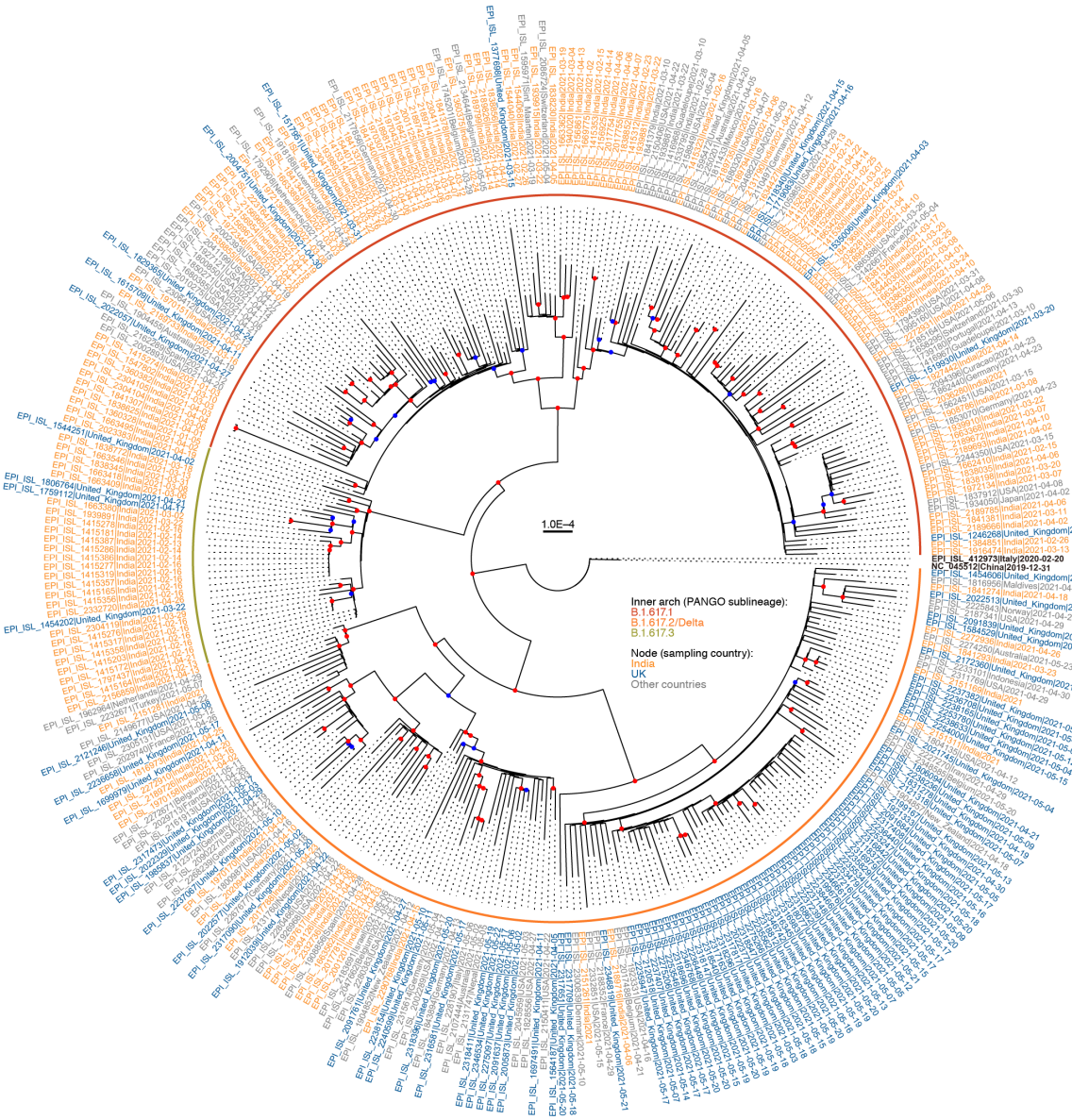

Extended Data Fig. 1. A maximum-likelihood based phylogenetic tree of the representative 334 SARS-CoV-2 sequences that belong to the B.1.617 lineage. GISAID ID, exposure country, and sampling date were noted in each terminal node. The country isolated (India, UK, or the other countries) and the PANGO sublineage are labeled by colors as indicated in the figure. Red or blue circle on the branch was shown in each internal node if the bootstrap value was ≥ 80 or ≥ 50 (n = 1,000).

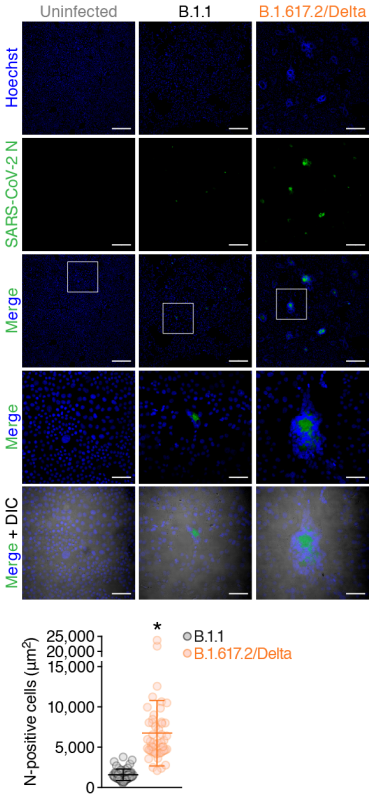

Extended Data Fig. 2. Immunofluorescence staining of B.1.617.2/Delta-infected VeroE6/TMPRSS2 cells.

VeroE6/TMPRSS2 cells infected with the viruses indicated [multiplicity of infection (MOI) 0.01] were stained with anti-SARS-CoV-2 nucleocapsid (N) (green) and Hoechst (blue). (Top) Representative images at 48 hpi are shown. Areas enclosed with squares are enlarged in the bottom panels. DIC, differential interference contrast. Bars, 200 μm for low magnification panels; 50 μm for high magnification panels. (Bottom) The area of N-positive cells in B.1.1-infected (n = 50) and B.1.617.2/Delta-infected (n = 50) cultures are shown. A statistically significant difference versus the B.1.1-infected culture (*, $P < 0.05$) was determined by the Mann-Whitney U test.

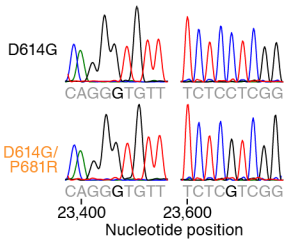

Extended Data Fig. 3. Chromatograms of the mutated regions of SARS-CoV-2 viruses artificially generated by reverse genetics.

Chromatograms of nucleotide positions 23,399-23,407 (left) and 23,600-23,608 (right) of parental SARS-CoV-2 (strain WK-521, PANGO lineage A; GISAID ID: EPI_ISL_408667) and the D614G (A23403G in nucleotide) and P681R (C23604G in nucleotide) mutation are shown.

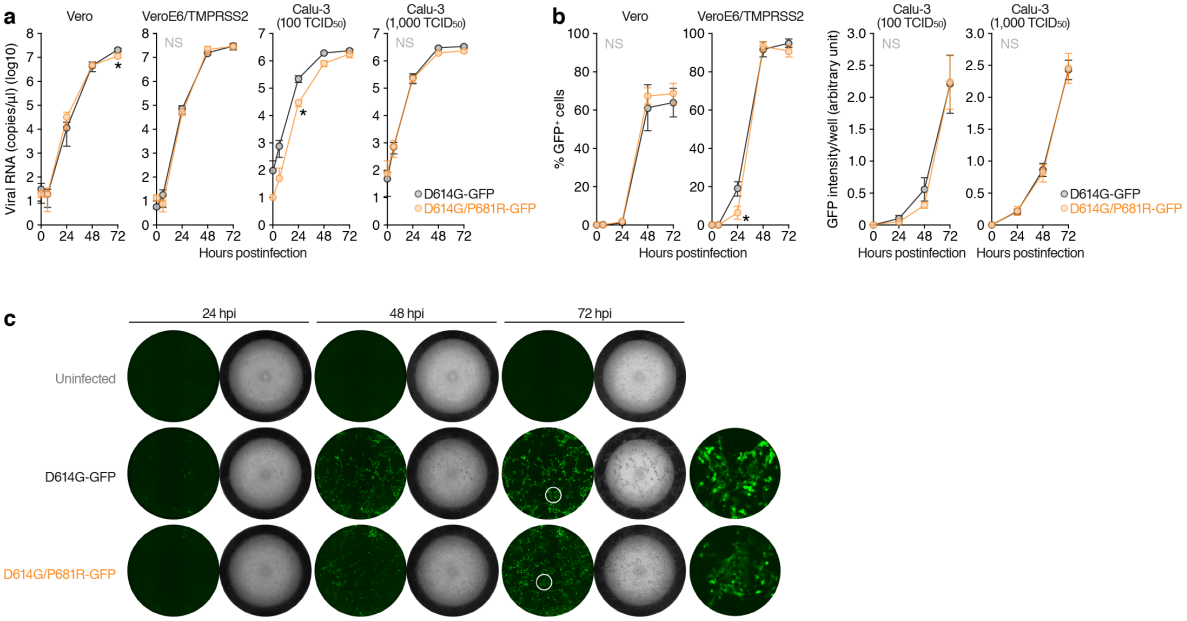

Extended Data Fig. 4. Growth kinetics of artificially generated GFP-expressing viruses.

The GFP-expressing D614G and D614G/P681R mutant viruses were generated by reverse genetics. These viruses (100 $TCID_{50}$ for Vero and VeroE6/TMPRSS2 cells, 100 or 1,000 $TCID_{50}$ for Calu-3 cells) were inoculated. The copy number of viral RNA in the culture supernatant (**a**) and the level of GFP-positive cells (the percentage of GFP-positive cells, for Vero and VeroE6/TMPRSS2 cells; the GFP intensity per well, for Calu-3 cells) (**b**) are shown. (**c**) Representative images of the Calu-3 cells infected with GFP-expressing viruses (100 $TCID_{50}$). Areas enclosed with circles are enlarged in the right panels. Assays were performed in quadruplicate. Statistically significant differences (*, $P < 0.05$) versus the D614G virus were determined by Student's *t* test. NS, no statistical significance.

686 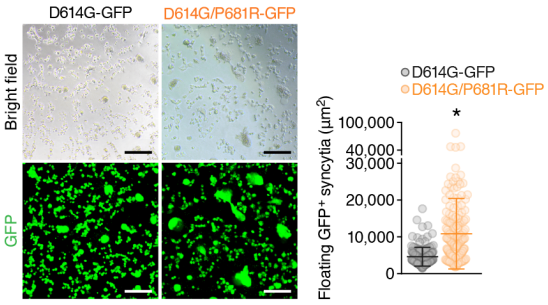

687

688 **Extended Data Fig. 5. Syncytia formation in VeroE6/TMPRSS2 cells infected**
689 **with GFP-expressing viruses.**
690 (Left) Floating syncytia in VeroE6/TMPRSS2 cells infected with the GFP-expressing
691 D614G and D614G/P681R mutant viruses (100 $TCID_{50}$) at 72 hpi are shown. Bars,
692 100 μm. (Right) The size of adherent GFP^+ syncytia in the D614G mutant-infected
693 (n = 147) and the D614G/P681R mutant-infected (n = 171) cultures are shown.
694 A statistically significant difference versus the D614G mutant-infected culture (*, $P <$
695 0.05) was determined by the Mann-Whitney U test.

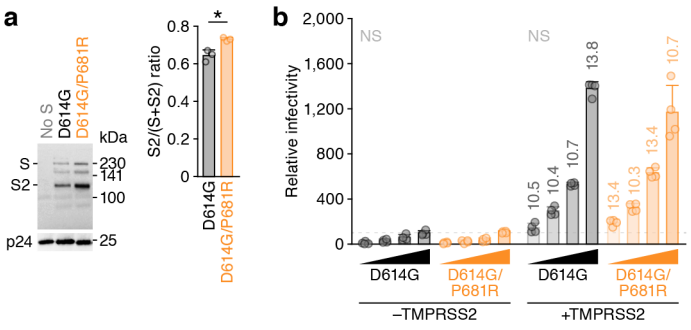

Extended Data Fig. 6. Infectivity of the P681R-bearing pseudovirus.
a, Western blotting of pseudoviruses. (Left) Representative blots of SARS-CoV-2 full-length S and cleaved S2 proteins as well as HIV-1 p24 capsid as an internal control. kDa, kilodalton. (Right) The ratio of S2 to the full-length S plus S2 proteins on pseudovirus particles.
b, Pseudovirus assay. The HIV-1-based reporter virus pseudotyped with the SARS-CoV-2 S D614G or D614G/P681R was inoculated into HOS-ACE2 cells or HOS-ACE2/TMPRSS2 cells at 4 different doses (125, 250, 500 and 1,000 ng HIV-1 p24 antigen). Percentages of infectivity compared to the virus pseudotyped with parental S D614G (1,000 ng HIV-1 p24) in HOS-ACE2 cells are shown. The numbers on the bars of the HOS-ACE2/TMPRSS2 cell data indicate the fold change versus the HOS-ACE2 cell data. Assays were performed in quadruplicate. NS, no statistical significance.

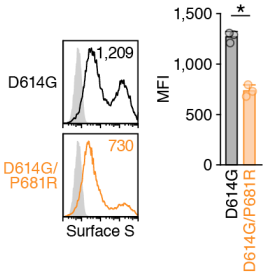

Extended Data Fig. 7. Flow cytometry of the S-expressing cells.
(Left) Representative histogram of the S protein expression on the cell surface. The number in the histogram indicates the mean fluorescence intensity (MFI). (Right) The MFI of surface S on the S-expressing cells. A statistically significant difference (*, $P < 0.05$) versus the D614G S was determined by Student's *t* test.

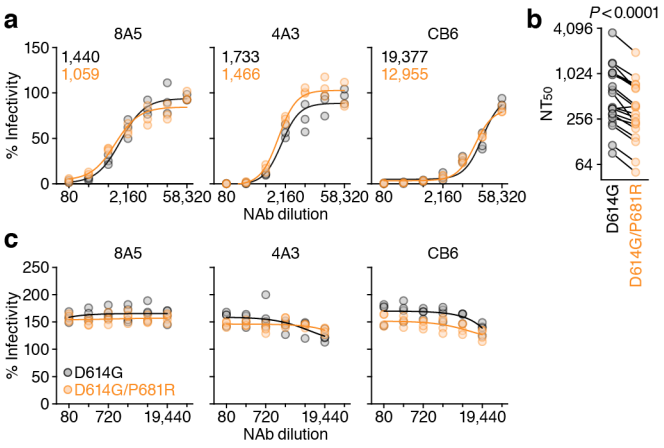

Extended Data Fig. 8. Association of the P681R mutation on the sensitivity to NAbs.

Neutralisation assay was performed by using three RBD-targeting monoclonal antibodies (clones 8A5, 4A3 and CB6) (**a** and **c**) and 19 vaccinated sera (**b**). NAbs were used for the pseudovirus assay (**a** and **b**) and the S-based fusion assay (**c**). Pseudoviruses and effector cells (S-expressing cells) were treated with serially diluted NAbs or sera as described in **Methods**. The raw data of panel **b** is shown in **Extended Data Fig. 9**. NT_{50}, 50% neutralisation titre.

In **a**, the NT_{50} values of the D614G S (black) and D614G/P681R S (orange) are indicated.

In **b**, a statistically significant difference versus the D614G virus was determined by Wilcoxon matched-pairs signed rank test.

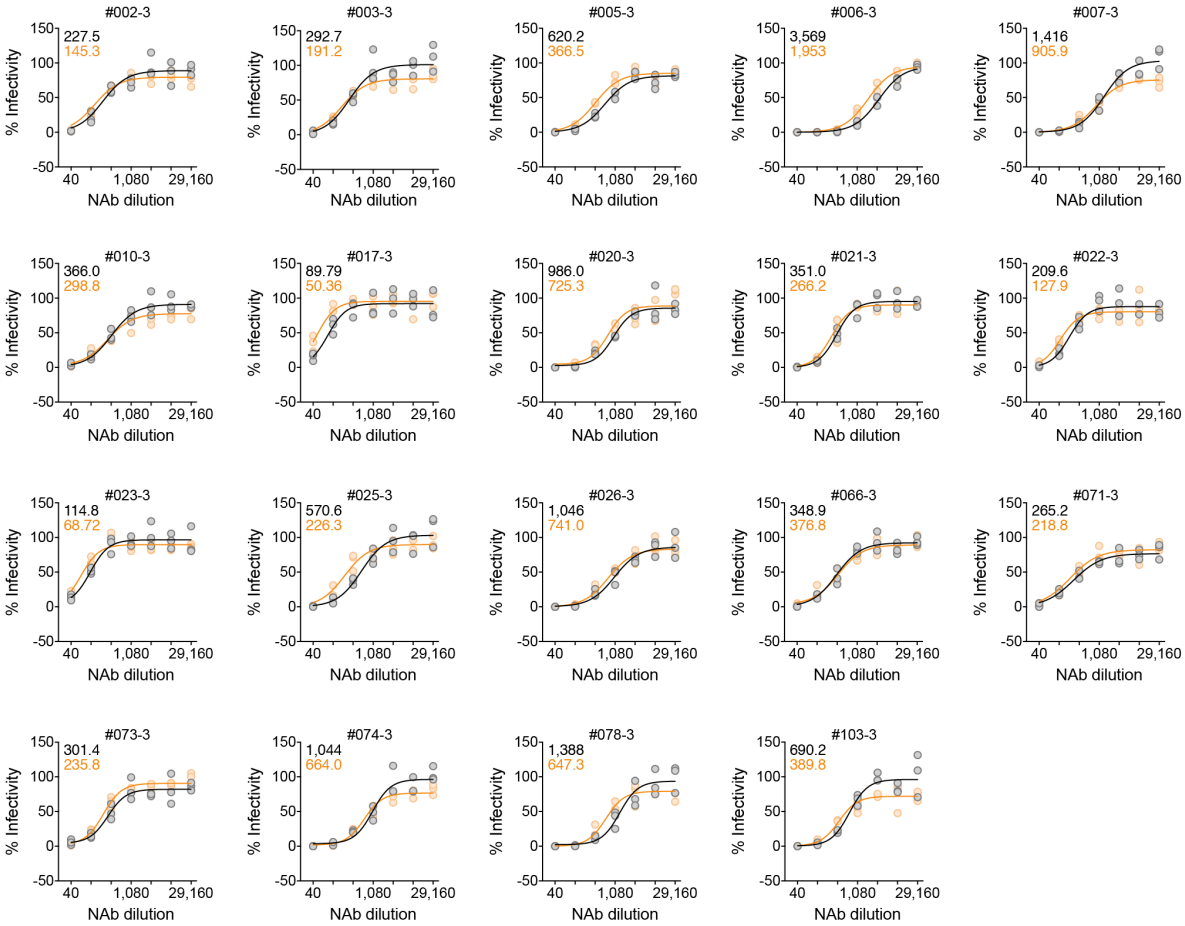

Extended Data Fig. 9. Neutralisation assay using 19 vaccinated sera. Nineteen vaccinated sera were used for the neutralisation assay. The NT_{50} values of respective serum against the D614G S (black) and D614G/P681R S (orange) are indicated in each panel. The NT_{50} values are summarized in **Extended Data Fig. 8b**.

739 **Extended Data Table 1.** Number of daily deposited sequences in GISAID.
740
741 **Extended Data Table 2.** Percentage of the mutations detected in the S protein of
742 the B.1.617 lineage.
743
744 **Extended Data Table 3.** The SARS-CoV-2 genomic region encoded by each
745 template and the primers used for the preparation of each fragment for CPER.

Methods

Ethics Statement

For virus isolation, this study was approved by the Institutional Review Board of Tokyo Metropolitan Institute of Public Health, according to the Declaration of Helsinki 2013 (approval number 3KenKenKen-466). For the use of human specimen, all protocols involving human subjects recruited at Kyoto University were reviewed and approved by the Institutional Review Boards of Kyoto University (approval number G0697). All human subjects provided written informed consent. All experiments with hamsters were performed in accordance with the Science Council of Japan's Guidelines for Proper Conduct of Animal Experiments. The protocols were approved by the Institutional Animal Care and Use Committee of National University Corporation Hokkaido University (approval number 20-0123) and the Animal Experiment Committee of the Institute of Medical Science, the University of Tokyo (approval number PA19-75).

Collection of BNT162b2-Vaccinated Sera

Peripheral blood were collected four weeks after the second vaccination of BNT162b2 (Pfizer-BioNTech), and the sera of 19 vaccinees (average age: 38, range: 28-59, 26% male) were isolated from peripheral blood. Sera were inactivated at 56°C for 30 min and stored at –80°C until use.

Cell Culture

HEK293 cells (a human embryonic kidney cell line; ATCC CRL-1573), HEK293T cells (a human embryonic kidney cell line; ATCC CRL-3216), and HOS cells (a human osteosarcoma cell line; ATCC CRL-1543) were maintained in Dulbecco's modified Eagle's medium (high glucose) (Wako, Cat# 044-29765) containing 10% fetal bovine serum (FBS) and 1% PS. Vero cells [an African green monkey (*Chlorocebus sabaeus*) kidney cell line; JCRB0111] were maintained in Eagle's minimum essential medium (Wako, Cat# 051-07615) containing 10% FBS and 1% PS. VeroE6/TMPRSS2 cells [an African green monkey (*Chlorocebus sabaeus*) kidney cell line; JCRB1819][37] were maintained in Dulbecco's modified Eagle's medium (low glucose) (Wako, Cat# 041-29775) containing 10% FBS, G418 (1 mg/ml; Nacalai Tesque, Cat# G8168-10ML) and 1% PS. Calu-3 cells (a human lung epithelial cell line; ATCC HTB-55) were maintained in Minimum essential medium Eagle (Sigma-Aldrich, cat# M4655-500ML) containing 10% FCS and 1% PS. HOS-ACE2/TMPRSS2 cells, the HOS cells stably expressing human ACE2, was prepared as described previously[8,38]. HEK293-C34 cells, the *IFNAR1* KO HEK293 cells

784 expressing human ACE2 and TMPRSS2 by doxycycline treatment[39], were
785 maintained in Dulbecco's modified Eagle's medium (high glucose) (Sigma-Aldrich,
786 Cat# R8758-500ML) containing 10% FBS, 10 μg/ml blasticidin (InvivoGen, Cat# ant-
787 bl-1) and 1% PS.
788
789 **Animal experiments**
790 Syrian hamsters (Male, 4 weeks old) were purchased from Japan SLC Inc.
791 (Shizuoka, Japan). Baseline body weights were measured before infection. For the
792 virus infection in **Fig. 2c, d**, hamsters were euthanised by intramuscular injection of
793 a mixture of 0.15 mg/kg medetomidine hydrochloride (Domitor®, Nippon Zenyaku
794 Kogyo), 2.0 mg/kg midazolam (Dormicum®, Maruishi Pharmaceutical) and 2.5 mg/kg
795 butorphanol (Vetorphale®, Meiji Seika Pharma). The B.1.1 or B.1.167.2/Delta viruses
796 (10^5 $TCID_{50}$ in 100 μl) was intranasally infected under anesthesia. Body weights were
797 measured and oral swabs were collected under anesthesia with isoflurane
798 (Sumitomo Dainippon Pharma) daily. For the virus infection in **Fig. 4**, four hamsters
799 per group were intranasally inoculated with the D614G or the D614G/P681R viruses
800 (10^4 $TCID_{50}$ in 30 μl) under isoflurane anesthesia. Body weight was monitored daily
801 for 7 days. For virological examinations, four hamsters per group were intranasally
802 infected with the D614G or the D614G/P681R viruses (10^4 $TCID_{50}$ in 30 μl); at 3 and
803 7 dpi, the animals were euthanized and nasal turbinates and lungs were collected.
804 The virus titers in the nasal turbinates and lungs were determined by use of plaque
805 assays on VeroE6/TMPRSS2 cells.
806
807 **Lung function**
808 Respiratory parameters were measured by using a whole-body plethysmography
809 system (PrimeBioscience) according to the manufacturer's instructions. In brief,
810 hamsters were placed in the unrestrained plethysmography chambers and allowed
811 to acclimatize for 1 m before data were acquired over a 3-min period by using
812 FinePointe software.
813
814 **Viral Genomes**
815 All SARS-CoV-2 genome sequences and annotation information used in this study
816 were downloaded from GISAID (https://www.gisaid.org) as of May 31, 2021
817 (1,761,037 sequences). We first excluded the genomes with non-human hosts. We
818 obtained SARS-CoV-2 variants belonging to the B.1.617 lineage based on the
819 PANGO annotation (i.e. sublineages B.1.617.1, B.1.617.2/Delta, or B.1.617.3) for
820 each sequence in the GISAID metadata. Note that only one variant belonging to the
821 B.1.617 lineage (GISAID ID: EPI_ISL_1544002 isolated in India on February 25,

822 2021) was not used in the analysis because the variant is not assigned any three
823 sublineages possibly due to 212 undetermined nucleotides in the genome. To infer
824 epidemiology of the B.1.617 lineage (**Fig. 1b-1f**), we excluded genomes that
825 sampling date information are not available, and collected 2,855, 13,821, or 83
826 sequences belonging to the B.1.617.1, B.1.617.2/Delta, or B.1.617.3 sublineage,
827 respectively.
828
829 **Phylogenetic Analyses**
830 To infer the phylogeny of the B.1.617 sublineages, we screened SARS-CoV-2
831 genomes by removing genomes containing undetermined nucleotides at coding
832 regions. Since the number of genomes belonging to the sublineage B.1.617.1 or
833 B.1.617.2/Delta are large (i.e. 894 or 6152 sequences, respectively), we used 150
834 sequences randomly chosen for each sublineage. For the B.1.617.3 sublineage, 32
835 genomes were used. We used Wuhan-Hu-1 strain isolated in China on December
836 31, 2019 (GenBank ID: NC_045512.2 and GISAID ID: EPI_ISL_402125) and LOM-
837 ASST-CDG1 strain isolated Italy on February 20, 2020 (GISAID ID:
838 EPI_ISL_412973) as an outgroup. We then collected 334 representative SARS-
839 CoV-2 sequences, and aligned entire genome sequences by using the FFT-NS-1
840 program in MAFFT suite v7.407[40]. All sites with gaps in alignment are removed, and
841 the total length of alignment is 29,085 nucleotides. Maximum likelihood tree was
842 generated by IQ-TREE 2 v2.1.3 software with 1,000 bootstraps[41]. GTR+G
843 substitution model is utilized based on BIC criterion.
844
845 **SARS-CoV-2 Preparation and Titration**
846 A B.1.617.2/Delta isolate (GISAID ID: EPI_ISL_2378732) and a D614G-bearing
847 B.1.1 isolate (GISAID ID: EPI_ISL_479681) were isolated from SARS-CoV-2-
848 positive individuals in Japan. Briefly, 100 µl of the nasopharyngeal swab obtained
849 from SARS-CoV-2-positive individuals were inoculated into VeroE6/TMPRSS2 cells
850 in the biosafety level 3 laboratory. After the incubation at 37°C for 15 minutes, a
851 maintenance medium supplemented with Eagle's minimum essential medium
852 (FUJIFILM Wako Pure Chemical Corporation, Cat# 056-08385) including 2% FBS
853 and 1% PS was added, and the cells were cultured at 37°C under 5% CO_2. The
854 cytopathic effect (CPE) was confirmed under an inverted microscope (Nikon), and
855 the viral load of the culture supernatant in which CPE was observed was confirmed
856 by real-time RT-PCR. To determine viral genome sequences, RNA was extracted
857 from the culture supernatant using QIAamp viral RNA mini kit (Qiagen, Qiagen, Cat#
858 52906) . cDNA library was prepared by using NEB Next Ultra RNA Library Prep Kit

859 for Illumina (New England Biolab, Cat# E7530) and whole genome sequencing was
860 performed by Miseq (Illumina).
861 To prepare the working virus, 100 µl of the seed virus was inoculated into
862 VeroE6/TMPRSS2 cells (5,000,000 cells in a T-75 flask). At one hour after infection,
863 the culture medium was replaced with Dulbecco's modified Eagle's medium (low
864 glucose) (Wako, Cat# 041-29775) containing 2% FBS and 1% PS; at 2-3 days
865 postinfection, the culture medium was harvested and centrifuged, and the
866 supernatants were collected as the working virus.
867 The titre of the prepared working virus was measured as 50% tissue culture
868 infectious dose ($TCID_{50}$). Briefly, one day prior to infection, VeroE6/TMPRSS2 cells
869 (10,000 cells/well) were seeded into a 96-well plate. Serially diluted virus stocks were
870 inoculated to the cells and incubated at 37°C for 3 days. The cells were observed
871 under microscopy to judge the CPE appearance. The value of $TCID_{50}$/ml was
872 calculated with the Reed–Muench method[42].
873
874 **SARS-CoV-2 Infection**
875 One day prior to infection, Vero cells (10,000 cells), VeroE6/TMPRSS2 cells (10,000
876 cells) and Calu-3 cells (10,000 cells) were seeded into a 96-well plate. SARS-CoV-
877 2 was inoculated and incubated at 37°C for 1 h. The infected cells were washed, and
878 180 µl of culture medium was added. The culture supernatant (10 µl) was harvested
879 at indicated time points and used for real-time RT-PCR to quantify the viral RNA
880 copy number. To monitor the syncytia formed in infected cell culture, the bright-field
881 photos were obtained using ECLIPSE Ts2 (Nikon). The size of floating syncytia was
882 measured by "quick selection tool" in Photoshop CS5 (Adobe) as pixel, and the area
883 of floating syncytia was calculated from the pixel value. As for the GFP-expressing
884 recombinant viruses (**Extended Data Fig. 4b, c**), the bright-field and green
885 fluorescence photos were obtained using an All-in-One Fluorescence microscope
886 BZ-X800 (Keyence) at the indicated time points, and the GFP-fluorescence intensity
887 was analyzed by a BZ-X800 Analyzer (Keyence).
888
889 **Immunofluorescence Staining**
890 One day prior to infection, VeroE6/TMPRSS2 cells (200,000 cells) were seeded on
891 the coverslips put in 12-well plate and were infected with SARS-CoV-2 (2,000
892 $TCID_{50}$). At 48 hours postinfection, the cells were fixed with 4% paraformaldehyde
893 in phosphate buffer saline (PBS) (Nacalai Tesque, Cat# 09154-85) for 10 min at
894 room temperature. The fixed cells were permeabilized with 0.1% Triton X-100 in PBS
895 for 10 min, blocked with 10% FBS in PBS for overnight at 4°C, and then stained
896 using mouse anti-SARS-CoV-2 N monoclonal antibody (GeneTex, Cat#

897 GTX632269) for 1 h. After washing three times with PBS, cells were incubated with
898 an Alexa 488-conjugated anti-mouse IgG antibody (Jackson ImmunoResearch, Cat#
899 015-540-003) for 1 h. Nuclei were stained with Hoechst 33342 (Thermo Fisher
900 Scientific, Cat# H3570). The coverslips were mounted on glass slides using
901 Fluoromount-G (Southern Biotechnology, Cat# 0100-01) with Hoechst 33342.
902 Fluorescence microscopy was performed on a confocal laser microscope (A1RSi,
903 Nikon) and captured with NIS-Elements AR software (Nikon). The area of N-positive
904 cells was quantified using Fiji software implemented in Image J.
905
906 **SARS-CoV-2 Reverse Genetics**
907 Recombinant SARS-CoV-2 was generated by circular polymerase extension
908 reaction (CPER) as previously described[39,43]. In brief, 9 DNA fragments encoding
909 the partial genome of SARS-CoV-2 (strain WK-521, PANGO lineage A; GISAID ID:
910 EPI_ISL_408667)[37] were prepared by PCR using PrimeSTAR GXL DNA polymerase
911 (Takara, cat# R050A). A linker fragment encoding hepatitis delta virus ribozyme,
912 bovine growth hormone polyA signal and cytomegalovirus promoter was also
913 prepared by PCR. The corresponding SARS-CoV-2 genomic region and the
914 templates and primers of this PCR are summarized in **Extended Data Table 3**. The
915 10 obtained DNA fragments were mixed and used for CPER[39]. To prepare the GFP-
916 expressing replication-competent recombinant SARS-CoV-2, the fragment 9 in
917 which the *GFP* gene was inserted in the *ORF7a* frame was used instead of the
918 authentic F9 fragment (see **Extended Data Table 3**)[39].
919 To produce recombinant SARS-CoV-2, the CPER products were
920 transfected into HEK293-C34 cells using TransIT-LT1 (Takara, cat# MIR2300)
921 according to the manufacturer's protocol. At one day posttransfection, the culture
922 medium was replaced with Dulbecco's modified Eagle's medium (high glucose)
923 (Sigma-Aldrich, cat# R8758-500ML) containing 2% FCS, 1% PS and doxycycline (1
924 μg/ml; Takara, cat# 1311N). At six days posttransfection, the culture medium was
925 harvested and centrifuged, and the supernatants were collected as the seed virus.
926 To remove the CPER products (i.e., SARS-CoV-2-related DNA), 1 ml of the seed
927 virus was treated with 2 μl TURBO DNase (Thermo Fisher Scientific, cat# AM2238)
928 and incubated at 37°C for 1 h. Complete removal of the CPER products (i.e., SARS-
929 CoV-2-related DNA) from the seed virus was verified by PCR. The working virus was
930 prepared by using the seed virus as described above.
931 To generate recombinant SARS-CoV-2 mutants, mutations were inserted
932 in fragment 8 (**Extended Data Table 3**) using the GENEART site-directed
933 mutagenesis system (Thermo Fisher Scientific, cat# A13312) according to the
934 manufacturer's protocol with the following primers: Fragment 8_S D614G forward,

935 5'-CCA GGT TGC TGT TCT TTA TCA GGG TGT TAA CTG CAC AGA AGT CCC
936 TG-3'; Fragment 8_S D614G reverse, 5'- CAG GGA CTT CTG TGC AGT TAA CAC
937 CCT GAT AAA GAA CAG CAA CCT GG -3'; Fragment 8_S P681R forward, 5'-AGA
938 CTC AGA CTA ATT CTC GTC GGC GGG CAC GTA GTG TA-3'; and Fragment 8_S
939 P681R reverse, 5'-TAC ACT ACG TGC CCG CCG ACG AGA ATT AGT CTG AGT
940 CT-3', according to the manufacturer's protocol. Nucleotide sequences were
941 determined by a DNA sequencing service (Fasmac), and the sequence data were
942 analyzed by Sequencher version 5.1 software (Gene Codes Corporation). The
943 CPER for the preparation of SARS-CoV-2 mutants was performed using mutated
944 fragment 8 instead of parental fragment 8. Subsequent experimental procedures
945 correspond to the procedure for parental SARS-CoV-2 preparation (described
946 above). To verify insertion of the mutation in the working viruses, viral RNA was
947 extracted using a QIAamp viral RNA mini kit (Qiagen, cat# 52906) and reverse
948 transcribed using SuperScript III reverse transcriptase (Thermo Fisher Scientific,
949 cat# 18080085) according to the manufacturers' protocols. DNA fragments including
950 the mutations inserted were obtained by RT-PCR using PrimeSTAR GXL DNA
951 polymerase (Takara, cat# R050A) and the following primers: WK-521 23339-23364
952 forward, 5'-GGT GGT GTC AGT GTT ATA ACA CCA GG-3'; and WK-521 24089-
953 24114 reverse, 5'-CAA ATG AGG TCT CTA GCA GCA ATA TC-3'. Nucleotide
954 sequences were determined as described above, and sequence chromatograms
955 (**Extended Data Fig. 3**) were visualized using the web application Tracy
956 (https://www.gear-genomics.com/teal/)[44].
957
958 **Real-Time RT-PCR**
959 Real-time RT-PCR was performed as previously described[43,45]. Briefly, 5 µl of culture
960 supernatant was mixed with 5 µl of 2 × RNA lysis buffer [2% Triton X-100, 50 mM
961 KCl, 100 mM Tris-HCl (pH 7.4), 40% glycerol, 0.8 U/µl recombinant RNase inhibitor
962 (Takara, cat# 2313B)] and incubated at room temperature for 10 min. RNase-free
963 water (90 µl) was added, and the diluted sample (2.5 µl) was used as the template
964 for real-time RT-PCR performed according to the manufacturer's protocol using the
965 One Step TB Green PrimeScript PLUS RT-PCR kit (Takara, cat# RR096A) and the
966 following primers: Forward *N*, 5'-AGC CTC TTC TCG TTC CTC ATC AC-3'; and
967 Reverse *N*, 5'-CCG CCA TTG CCA GCC ATT C-3'. The copy number of viral RNA
968 was standardized with a SARS-CoV-2 direct detection RT-qPCR kit (Takara, cat#
969 RC300A). The fluorescent signal was acquired using a QuantStudio 3 Real-Time
970 PCR system (Thermo Fisher Scientific), a CFX Connect Real-Time PCR Detection
971 system (Bio-Rad), an Eco Real-Time PCR System (Illumina) or a 7500 Real Time
972 PCR System (Applied Biosystems).

973
974 **Plasmid Construction**
975 A plasmid expressing the SARS-CoV-2 S D614G protein was prepared in our
976 previous study[8]. A plasmid expressing the SARS-CoV-2 S D614G/P681R mutant
977 was generated by site-directed mutagenesis PCR using pC-SARS2-S D614G[8] as
978 the template and the following primers: P681R Fw, 5'- CCA GAC CAA CAG CCG
979 GAG GAG GGC AAG GTC T-3' and P681R Rv, 5'-AGA CCT TGC CCT CCT CCG
980 GCT GTT GGT CTG G-3'. The resulting PCR fragment was digested with KpnI and
981 NotI and inserted into the KpnI-NotI site of the pCAGGS vector[46].
982
983 **Pseudovirus Assay**
984 Pseudovirus assay was performed as previously described[8,43]. Briefly, the
985 pseudoviruses, lentivirus (HIV-1)-based, luciferase-expressing reporter viruses
986 pseudotyped with the SARS-CoV-2 S protein and its derivatives, HEK293T cells (1
987 × 10^6 cells) were cotransfected with 1 μg of psPAX2-IN/HiBiT[47], 1 μg of pWPI-Luc2[47],
988 and 500 ng of plasmids expressing parental S or its derivatives using Lipofectamine
989 3000 (Thermo Fisher Scientific, Cat# L3000015) or PEI Max (Polysciences, Cat#
990 24765-1) according to the manufacturer's protocol. At two days posttransfection, the
991 culture supernatants were harvested, centrifuged. The amount of pseudoviruses
992 prepared was quantified using the HiBiT assay as previously described[8,47]. The
993 pseudoviruses prepared were stored at –80°C until use. For the experiment, HOS-
994 ACE2 cells and HOS-ACE2/TMPRSS2 cells (10,000 cells/50 μl) were seeded in 96-
995 well plates and infected with 100 μl of the pseudoviruses prepared at 4 different
996 doses. At two days postinfection, the infected cells were lysed with a One-Glo
997 luciferase assay system (Promega, Cat# E6130), and the luminescent signal was
998 measured using a CentroXS3 plate reader (Berthhold Technologies) or GloMax
999 explorer multimode microplate reader 3500 (Promega).
1000
1001 **Western blotting**
1002 Western blotting was performed as previously described[48-50]. To quantify the level of
1003 the cleaved S2 protein in the cells, the harvested cells were washed and lysed in
1004 lysis buffer [25 mM HEPES (pH 7.2), 20% glycerol, 125 mM NaCl, 1% Nonidet P40
1005 substitute (Nalacai Tesque, Cat# 18558-54), protease inhibitor cocktail (Nalacai
1006 Tesque, Cat# 03969-21)]. After quantification of total protein by protein assay dye
1007 (Bio-Rad, Cat# 5000006), lysates were diluted with 2 × sample buffer [100 mM Tris-
1008 HCl (pH 6.8), 4% SDS, 12% β-mercaptoethanol, 20% glycerol, 0.05% bromophenol
1009 blue] and boiled for 10 min. Ten microliter of the samples (50 μg of total protein)
1010 were subjected to western blotting. To quantify the level of the cleaved S2 protein

1011 on virions, 900 µl of the culture medium including the pseudoviruses were layered
1012 onto 500 µl of 20% sucrose in PBS and centrifuged at 20,000 × g for 2 h at 4°C.
1013 Pelleted virions were resuspended in 1× NuPAGE LDS sample buffer (Thermo
1014 Fisher Scientific, Cat# NP0007) containing 2% β-mercaptoethanol, and the lysed
1015 virions were subjected to western blotting. For the protein detection, following
1016 antibodies were used: mouse anti-SARS-CoV-2 S monoclonal antibody (clone 1A9,
1017 GeneTex, Cat# GTX632604), rabbit anti-ACTB monoclonal antibody (clone 13E5,
1018 Cell Signaling, Cat# 4970), mouse anti-HIV-1 p24 monoclonal antibody (clone 183-
1019 H12-5C, obtained from the HIV Reagent Program, NIH, Cat# ARP-3537),
1020 horseradish peroxidase (HRP)-conjugated donkey anti-rabbit IgG polyclonal
1021 antibody (Jackson ImmunoResearch, Cat# 711-035-152), and HRP-conjugated
1022 donkey anti-mouse IgG polyclonal antibody (Jackson ImmunoResearch, Cat# 715-
1023 035-150). Chemiluminescence was detected using SuperSignal West Femto
1024 Maximum Sensitivity Substrate (Thermo Fisher Scientific, Cat# 34095) or Western
1025 BLoT Ultra Sensitive HRP Substrate (Takara, Cat# T7104A) according to the
1026 manufacturers' instruction. Bands were visualized using the image analyzer,
1027 Amersham Imager 600 (GE Healthcare), and the band intensity was quantified using
1028 Image Studio Lite (LI-COR Biosciences) or Image J.
1029
1030 **SARS-CoV-2 S-Based Fusion Assay**
1031 The SARS-CoV-2 S-based fusion assay was performed as previously described[43].
1032 This assay utilizes a dual split protein (DSP) encoding *Renilla* luciferase (RL) and
1033 *GFP* genes, and the respective split proteins, DSP_{1-7} and DSP_{8-11}, are expressed in
1034 effector and target cells by transfection[49,51]. Briefly, on day 1, effector cells (i.e., S-
1035 expressing cells) and target cells (i.e., ACE2-expressing cells) were prepared at a
1036 density of 0.6 to 0.8 × 10^6 cells in a 6 well plate. To prepare effector cells, HEK293
1037 cells were cotransfected with the expression plasmids for D614G S or D614G/P681R
1038 (400 ng) with $pDSP_{1-7}$ (400 ng) using TransIT-LT1 (Takara, Cat# MIR2300). To
1039 prepare target cells, HEK293 cells were cotransfected with pC-ACE2 (200 ng) and
1040 $pDSP_{8-11}$ (400 ng). In addition to the plasmids above, selected wells of target cells
1041 were also cotransfected with pC-TMPRSS2 (40 ng). On day 3 (24 h posttransfection),
1042 16,000 effector cells were detached and reseeded into 96-well black plates
1043 (PerkinElmer, Cat# 6005225), and target cells were reseeded at a density of
1044 1,000,000 cells/2 ml/well in 6-well plates. On day 4 (48 h posttransfection), target
1045 cells were incubated with EnduRen live cell substrate (Promega, Cat# E6481) for 3
1046 h and then detached, and 32,000 target cells were applied to a 96-well plate with
1047 effector cells. RL activity was measured at the indicated time points using a Centro
1048 XS3 LB960 (Berthhold Technologies). The S proteins expressed on the surface of

1049 effector cells were stained with rabbit anti-SARS-CoV-2 S monoclonal antibody
1050 (GeneTex, Cat# GTX635654) and APC-conjugated goat anti-rabbit IgG polyclonal
1051 antibody (Jackson ImmunoResearch, Cat# 111-136-144). Normal rabbit IgG
1052 (SouthernBiotech, Cat# 0111-01) was used as a negative control. Expression levels
1053 of surface S proteins were analyzed using a FACS Canto II (BD Biosciences). RL
1054 activity was normalized to the mean fluorescence intensity (MFI) of surface S
1055 proteins, and the normalized values are shown as fusion activity.
1056
1057 **Mathematical Modeling for Fusion Velocity Quantification**
1058 The following cubic polynomial regression model was employed to fit each of time-
1059 series datasets (**Fig. 3e**):
1060 $$y \sim b_0 + b_1 x + b_2 x^2 + b_3 x^3$$
1061 The initial velocity of cell fusion was estimated from the derivative of the fitted cubic
1062 curve.
1063
1064 **Neutralisation Assay**
1065 Virus neutralisation assay was performed on HOS-ACE2/TMPRSS2 cells using the
1066 SARS-CoV-2 S pseudoviruses expressing luciferase (see "Pseudovirus Assay"
1067 above). The viral particles pseudotyped with D614G S or D614G/P681R S were
1068 incubated with serial dilution of heat-inactivated human serum samples or the RBD-
1069 targeting NAbs (clones 8A5, 4A3 and CB6; Elabscience) at 37°C for 1 h. The
1070 pseudoviruses without sera and NAbs were also included. Then, the 80 μl mixture
1071 of pseudovirus and sera/NAbs was added into HOS-ACE2/TMPRSS2 cells (10,000
1072 cells/50 μl) in a 96-well white plate and the luminescence was measured as
1073 described above (see "Pseudovirus Assay" above). 50% neutralisation titre (NT_{50})
1074 was calculated using Prism 9 (GraphPad Software).
1075 For the cell-cell fusion neutralisation assay, effector cells of the S-based
1076 fusion assay (i.e., S-expressing cells) were incubated with the serially diluted
1077 neutralizing antibodies targeting RBD (clones 8A5, 4A3 and CB6; Elabscience) at
1078 37°C for 1 h. Then, target cells were applied and performed the S-based fusion
1079 assay as described above (see "SARS-CoV-2 S-Based Fusion Assay" above).